Hindawi Publishing Corporation
EURASIP Journal on Advances in Signal Processing
Volume 2010, Article ID 895486, 14 pages
doi:10.1155/2010/895486

Research Article

A Machine Learning Approach for Locating Acoustic Emission

N. F. Ince,[1] Chu-Shu Kao,[2] M. Kaveh,[1] A. Tewfik (EURASIP Member),[1] and J. F. Labuz[2]

[1] *Department of Electrical and Computer Engineering, University of Minnesota, Minneapolis, MN 55455, USA*
[2] *Department of Civil Engineering, University of Minnesota, Minneapolis, MN 55455, USA*

Correspondence should be addressed to N. F. Ince, ince_firat@yahoo.com

Received 18 January 2010; Revised 26 July 2010; Accepted 20 October 2010

Academic Editor: João Marcos A. Rebello

Copyright © 2010 N. F. Ince et al. This is an open access article distributed under the Creative Commons Attribution License, which permits unrestricted use, distribution, and reproduction in any medium, provided the original work is properly cited.

This paper reports on the feasibility of locating microcracks using multiple-sensor measurements of the acoustic emissions (AEs) generated by crack inception and propagation. Microcrack localization has obvious application in non-destructive structural health monitoring. Experimental data was obtained by inducing the cracks in rock specimens during a surface instability test, which simulates failure near a free surface such as a tunnel wall. Results are presented on the pair-wise event correlation of the AE waveforms, and these characteristics are used for hierarchical clustering of AEs. By averaging the AE events within each cluster, "super" AEs with higher signal to noise ratio (SNR) are obtained and used in the second step of the analysis for calculating the time of arrival information for localization. Several feature extraction methods, including wavelet packets, autoregressive (AR) parameters, and discrete Fourier transform coefficients, were employed and compared to identify crucial patterns related to P-waves in time and frequency domains. By using the extracted features, an SVM classifier fused with probabilistic output is used to recognize the P-wave arrivals in the presence of noise. Results show that the approach has the capability of identifying the location of AE in noisy environments.

1. Introduction

Rapidly changing environmental conditions and harsh mechanical loading are sources of damage to structures. Resulting damage can be examined based on local identification such as the presence of small cracks (microcracks) in a component or global identification such as changes in natural frequency of the structure. Continuous health monitoring process may involve both global and local identification. Generally, local damage, such as cracks in critical components, is inspected visually. This type of inspection is slow and prone to human error. Therefore, automated, fast, and accurate techniques are needed to detect the onset of local damage in critical components to prevent failure.

In this scheme, nondestructive testing and monitoring should be employed so that the damage can be inferred through analysis of the signals obtained from inspection. Acoustic emission (AE) events can serve as a source of information for locating the damage, particularly as caused by the initiation and propagation of microcracks [1–3]. The spatial distribution of AE locations can provide clues about the position and extent of the damage [4]. In practice, the location of AE is estimated from the primary wave (P-wave), the first part of the signal to arrive at the sensor (see Figure 2(c)). However, the use of AE waveforms is often obscured by noise and spurious events, which may cause misinterpretation of the data. Even in controlled laboratory settings, it is difficult to account for all the sources of noise. Therefore, an AE system that automatically "learns" crucial patterns from the total AE data, as well as particular P-wave arrivals, may provide clues for distinguishing between real events and extraneous signals, thus improving the spatial accuracy of AE locations and reduce false alarms. Accurate detection of these events with appropriate signal processing and machine learning techniques may open new possibilities for monitoring the health of critical components; this offers the possibility for raising alarms in an automated manner if the degradation of structural integrity is severe.

In this paper, we describe a novel combination of signal processing and machine learning techniques based on hierarchical clustering and support vector machines to process multi-sensor AE data generated by the inception and propagation of microcracks in rock specimens during a surface instability test. The effectiveness of the approach is validated

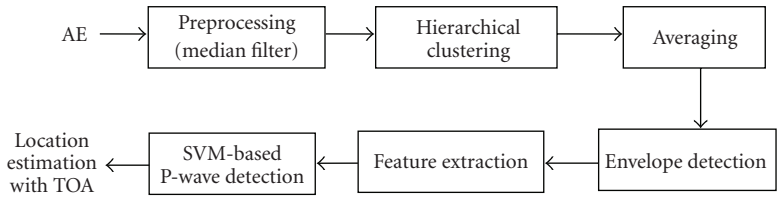

Figure 1: Schematic diagram of the signal processing and classification system. The AE signals were preprocessed with a median filter. In the following step they are grouped with a hierarchical clustering procedure. An averaging step was implemented in each cluster to improve the SNR. This is followed by a feature extraction procedure in time and frequency domains. On the test data, the feature extraction and classification steps were executed when the signal envelope exceeded a predefined threshold. The TOA is calculated by detecting the P-waves with an SVM classifier.

by laboratory-based experimental results. Fundamental to the proposed technique is experimentally observed highly correlated AE waveforms that are generated by the propagation of microcracks [3]. A similar phenomenon was also reported in [5] by exploring the use of coherence functions in the frequency domain. Thus, the signal processing framework we present in this study focuses on the capture and processing of such correlated events as representing signals of interest for damage localization. The correlated nature of these events is expected to be different from extraneous interfering signals within the same measurement bandwidth that may be generated by other mechanisms with random characteristics. Several features were extracted from time and frequency domain using autoregressive modeling, wavelet packets (WP), and discrete Fourier transform. These features were used in conjunction with a maximum margin support vector machine (SVM) classifier coupled with probabilistic output [6] to recognize the P-waves in the presence of noise for accurate time of arrival (TOA) calculation. The classification step is followed by the use of TOA information of the identified waves of interest for estimating the location of the microcracks. The feasibility of the proposed techniques in determining the location of a fracture is presented by examining AE events recorded by eight sensors attached to a structure with localized microcracks. A block diagram summarizing the overall signal processing system is given in Figure 1.

The remainder of the paper is organized as follows. In the next section, the experiments and the AE data sets recorded from two specimens during controlled failure tests are described. Next, the signal preprocessing techniques used for enhancing the measured AE signals in the presence of noise and data acquisition imperfections are presented. This is followed by a description of a novel hierarchical clustering technique to group the AE events. The feature extraction and machine learning techniques for detecting P-waves are described in Section 4. Finally, the experimental results on the spatial distributions of AE events are provided and compared to the actual fracture locations.

2. Acoustic Emission Recordings

AE events were recorded during a surface instability test that is used to examine failure near a free surface such as a tunnel wall. A photo representing the experimental setup

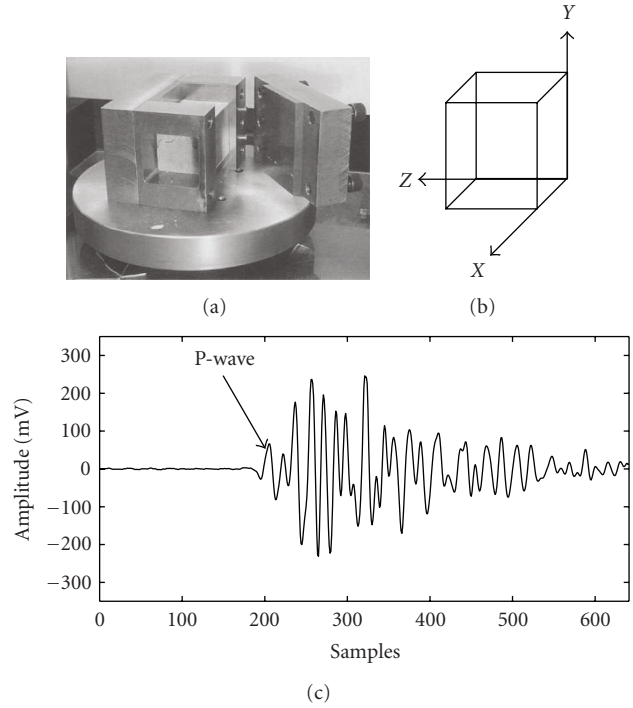

Figure 2: (a) Experimental setup for recording the AE events in a surface instability test. (b) Coordinate axes of the setup. (c) AE event recorded from the first sensor that triggers the data acquisition process. The P-wave is indicated with an arrow; it is the first component that arrives at the sensor and used for time of arrival detection.

is given in Figure 2. A prismatic rock specimen, wedged between two rigid vertical side walls and a rigid vertical rear wall, is subjected to axial load applied in the Y-direction through displacing rigid platens. The specimen is supported in the Z-direction such that compressive stress is generated passively. The rear wall in X-direction ensures that the lateral deformation and failure (cracks) were promoted to take place on the front, exposed face of the specimen.

Four acoustic emission (AE) sensors were attached to the exposed face using cyanoacrylate glue, and their positions (x, y, z) were measured. Four other AE sensors were fastened to the side walls of the apparatus. The AE data were collected with high-speed, CAMAC-based data acquisition

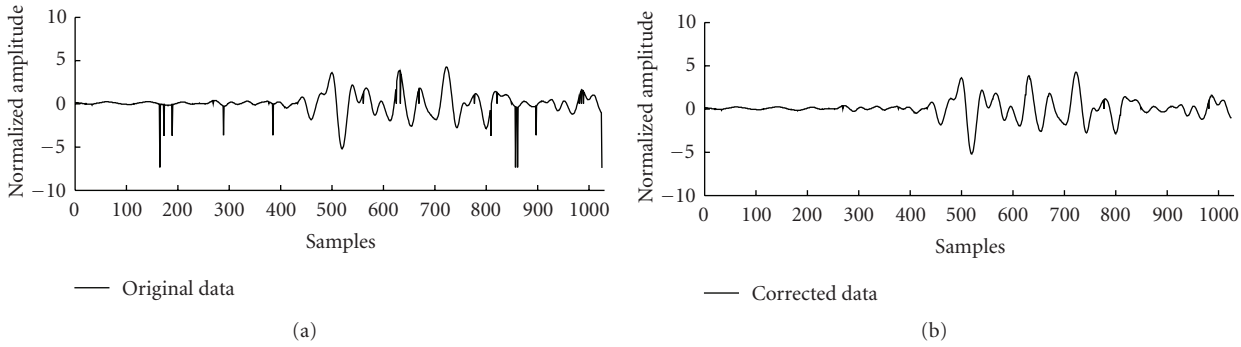

Figure 3: Original signal on (a) corrupted with spikes. At (b), the corrected signal with a median filter.

equipment, consisting of four two-channel modular transient recorders (LeCroy model 6840) with 8-bit analog to digital converter (ADC) resolution and a sampling rate of 20 MHz. The data acquisition system was interfaced with eight piezoelectric transducers (Physical Acoustics model S9225), and eight preamplifiers with bandpass filters from 0.1 to 1.2 MHz and 40 dB gain were used for conditioning the raw AE signals. The frequency response of these transducers ranged from 0.1 to 1 MHz, with a diameter of approximately 3 mm. All channels were triggered when the signal amplitude exceeded a certain threshold on the first sensor. This sensor is referred to as the "anchor" sensor. AE data were acquired in a more or less continuous fashion until 128 Kbytes of a digitizer memory were filled; then the AE data were transferred to the host computer, with approximately four seconds of downtime. The entire waveforms were stored automatically and sequentially with a time stamp. This experiment was repeated twice using two very similar rock specimens with dimensions of 62 mm $(X) \times 93$ mm $(Y) \times 80$ mm (Z) labeled as SR1 and SR2. A sample AE signal recorded with the system is presented in Figure 2(c). In total, 2176 and 1536 AE events were recorded in the experiments SR1 and SR2, respectively. This number includes both real AE and spurious (noise) events.

Several events contained spikes (Figure 3), which probably originated from ADC sign errors. Consequently, a median filter was employed to remove the spikes from the AE recordings. The median filter is a nonlinear digital filtering technique that has found widespread application in image processing. In this study, each sample was replaced with the median value of a window covering three pre- and post-samples. A representative corrupted signal and median filter output is shown in Figure 3. The median filter successfully corrected the events with consecutive spikes.

3. Clustering of AE Events

In practice, the crack locations are inspected visually by projecting on a plane the locations of individual AE events, which are estimated from the TOA information at the sensors [7]. The TOA is determined by comparing the signal amplitude to a predefined threshold, where the earliest arrival is due to the P-wave, as shown in Figures 2 and 4(a). This type of method produces misleading TOA information if the signal is noisy, which is usually the case in actual structures. For instance, the data set we recorded contained several records with corrupted baseline (Figure 4(b)) or pseudo-AE events. Therefore, before applying the amplitude threshold, the SNR of the signal was increased by capturing correlated recordings and averaging grouped events. For this particular purpose, a hierarchical clustering approach, which uses the cross-correlation function computed between different events, was applied.

As a first step, the normalized cross-correlation function $R_{xy}[k]$ was computed for only 256 shifts between pairs of events represented by the preprocessed signals $x[n]$ and $y[n]$ acquired at the anchor sensor:

$$R_{xy}[k] = \frac{1}{(N-k)\sigma_x\sigma_y}\sum_n x[n]y[n+k], \quad |k| \le 256. \tag{1}$$

A correlation matrix was then constructed using the maximum value of the absolute cross-correlation function between all event pairs. The lag indices of maximum correlation between paired events were saved to align the associated events in further steps of the analysis. The correlation matrices of the two data sets are shown in Figure 5. These correlation matrices were used to build a hierarchical cluster [8]. The average linkage method was used to build the dendrogram, which represented the nested correlation structure of all AE events. The dendrogram was cut at level 0.2 in order to cluster those events that have average cross-correlations equal or larger than 0.8. At this level, 105 and 80 clusters were obtained with two or more members for SR1 and SR2, respectively.

AE events related to a particular cluster with four members are shown in Figure 5. This step was followed by computing the averages of each cluster to obtain "super" AE signals. In this scheme, averaging is expected to reduce the uncorrelated noise in comparison with the repetitive AE signal component across the records of a given cluster, resulting in an amplitude SNR increase of at best $\sqrt{C}$, where C is the number of events in a cluster. A similar approach has been utilized for processing gene expression profiles in [9]; it has been shown that averaged gene expression data within clusters have more predictive power than those from individual gene expressions. Thus, by increasing the SNR of the waveforms, AE locations will be more accurate.

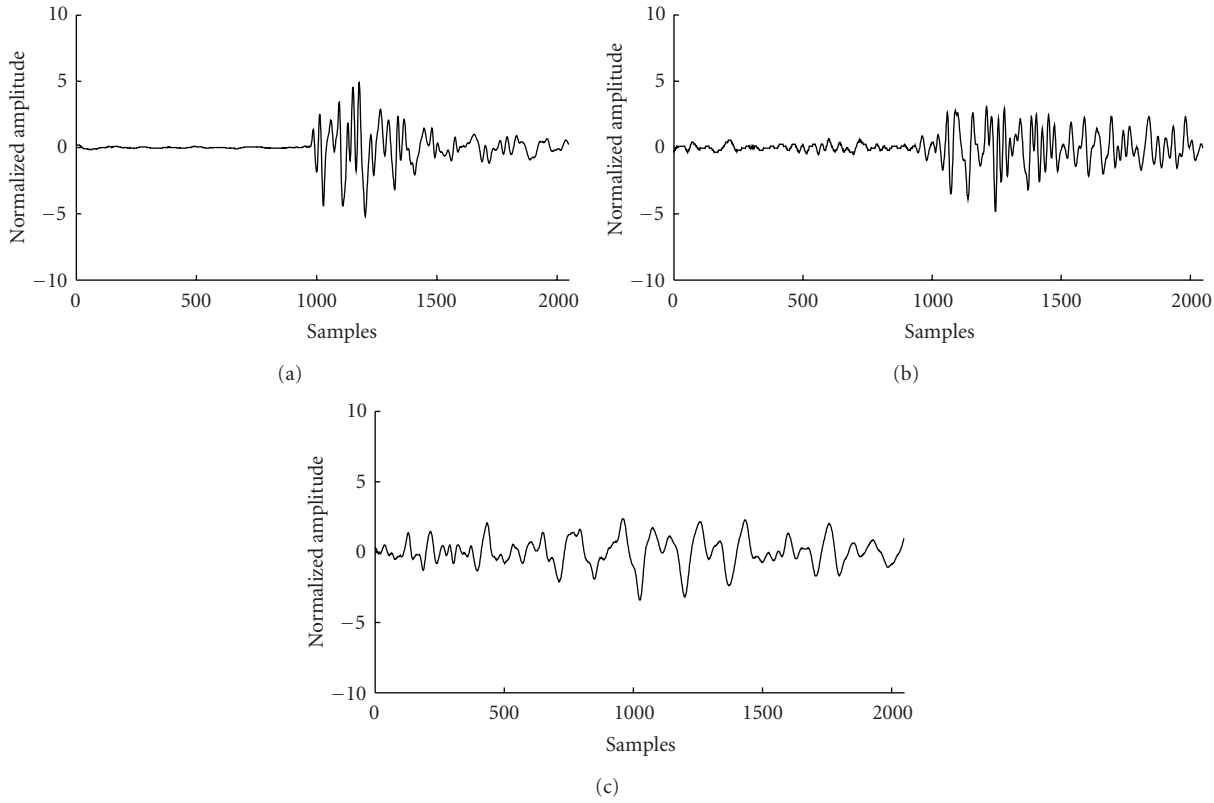

Figure 4: Sample AE recordings. (a) High SNR with clear baseline. (b) Corrupted baseline. (c) Pseudo-AE (noise).

In order to improve the amplitude SNR by a factor of two or more, clusters with at least four members were used in estimating the location of AE. Those clusters with large numbers of members increase the reliability of the location estimation step. We emphasize that the key assumption here, and one that has been observed experimentally, is the very low likelihood that, in practice, noise will also be highly correlated across multiple measurement records. Hence, it is expected that highly correlated signals (events) can only originate from a source such as microcracks.

4. P-Wave Detection with SVM

The spatial distribution of AE is estimated from the TOA information, which is extracted from the waveforms. The detection of P-waves by a using simple threshold becomes difficult in the presence of noise or local peaks in the data. With lower amplitude thresholds, the rate of false positives (FP) increases rapidly due to the noise in the baseline. Increasing the amplitude threshold may cause a decrease in false positive along with the true positive (TP) rate. Consequently, an intelligent algorithm is needed to distinguish between real and pseudo-P-waves (noise). In this paper, the use of a maximum margin classifier using input features extracted from time and frequency domain analysis of the AE data was investigated for the detection of the P-waves. In order to determine the TOA accurately, the time and frequency domain properties of the AE data in short windows around the P-wave arrival were examined. The energy of P-waves was generally found to be located in lower frequency bands. This wave was followed by large oscillations with similar spectral characteristic (the 1st row in Figure 6(a)). Sample waveforms and spectra related to a typical P-wave (center frame in the 1st row, Figure 6(a)) and those windows preceding and following this wave are presented in frames 1 and 3 in Figure 6(a). The same analysis related to a segment that may be recognized as a pseudo-P-wave is also given (Figure 6(b)). It is observed that the pseudo-P-waves *were not* followed by large oscillations. In addition, their frequency spectrum indicates that these waveforms had a certain amount of energy in mid-frequency bands. In the following, we describe three approaches for determining features to be used in a classifier. The identification of the features was implemented on a training set by selecting around 20 multichannel "super" AE events from each data set. The effectiveness of these features and their combinations are examined on testing datasets in Section 5.

4.1. Discrete Fourier Transform-Based Features. Based on the above observations on the frequency characteristics of P-waves and noise and within the spirit of [10], so-called Mel Scale, subband energy features were extracted from the spectrum of each time window using a fast Fourier transform. A Blackman-Tukey window was used during the estimation of spectra of segments. In total, five subbands

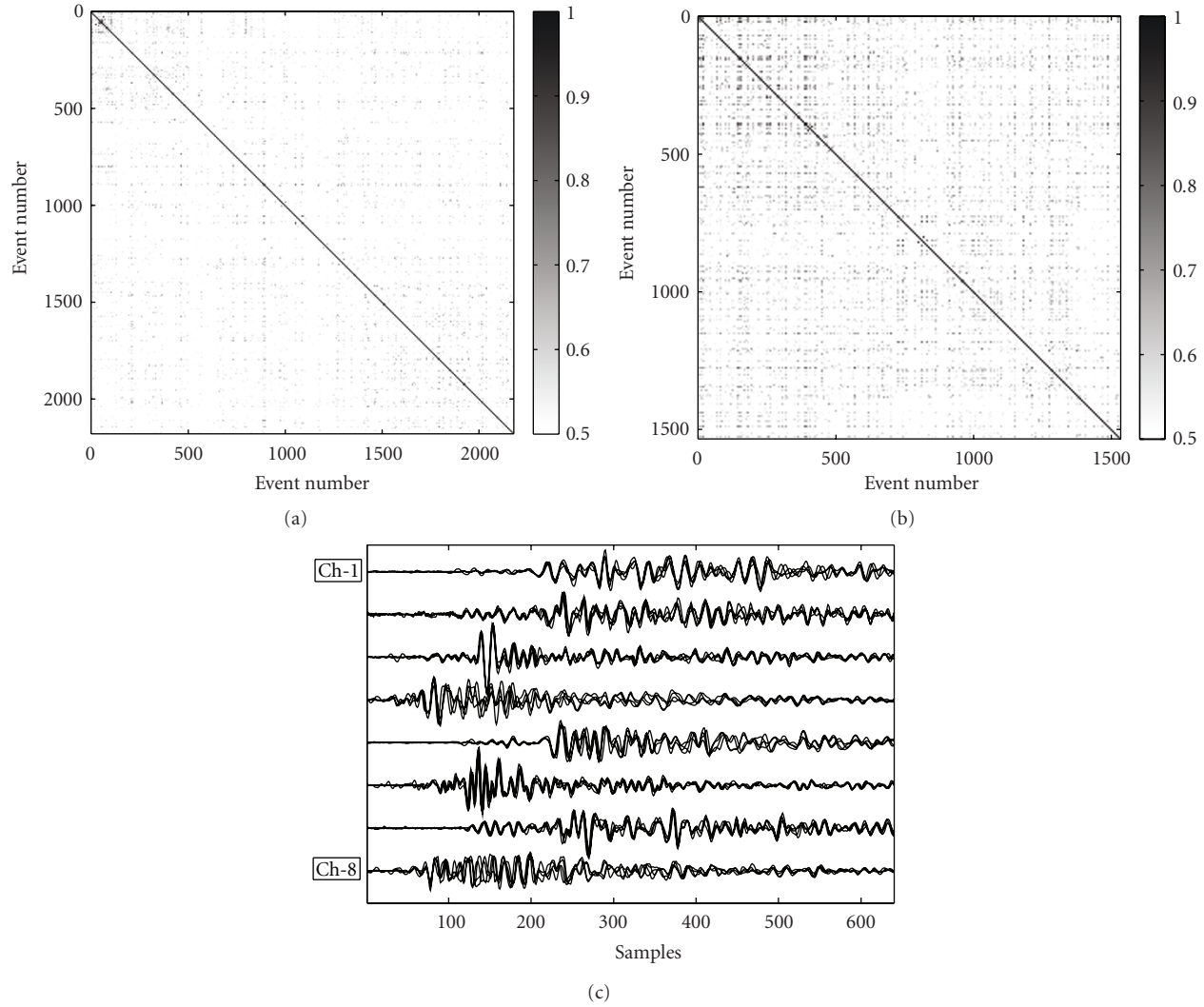

Figure 5: Correlation matrices of (a) SR1 and (b) SR2. (c) Overlap plot of AE events related to a particular cluster with four members.

were extracted. The widths of the subbands were not uniform and had a dyadic structure. The lowest two bands had the same bandwidth, and the following subbands were twice as wide as the preceding subbands. This setup focused more on the lower frequency bands since the energy of the signal was concentrated in this range. By concatenating the Mel Scale subband features from all three windows, a 15-dimensional feature vector was constructed. Generally, the noise (pseudo-P-waves) had jagged spectra. In contrast, the spectra of the P-waves were smooth. The variance of the derivative of the spectrum of each time window was also computed as another feature to capture this difference.

4.2. Discriminatory Wavelet Packet Analysis-Based Features. In addition to the energies computed in predefined Mel Scale subbands, we also considered selection of the subbands adaptively with a discriminant wavelet packet (WP) analysis technique [11]. In more detail, the signals belonging to noise and P-waves are decomposed into WP coefficients over a pyramidal tree structure. In the following step, the expansion coefficients at each position in the tree structure are squared and averaged within each class. Then a Euclidean distance between the averaged expansion coefficients of noise and P-waves were computed at each node of the WP tree. The corresponding binary tree structure was pruned from bottom to top to select the most discriminatory frequency subbands. This is achieved by comparing the estimated distance of the children and mother nodes. The energy, in each selected band, is used as a feature for the recognition of P-waves. The reader is referred to [11, 12] for a detailed description of discriminatory wavelet packet analysis and its derivations. Since short data segments are inspected, we used a four-tap Daubechies wavelet filter while analyzing the signals. A tree depth of four was selected, where in the finest level the available bandwidth was divided in 16 subbands. In Figure 7, we present the selected WP subbands for the datasets SR1 and SR2, respectively. We note that the obtained segmentations were somewhat similar in both datasets. Wider subbands were selected in the left window preceding the P-wave. We note that the entire high frequency

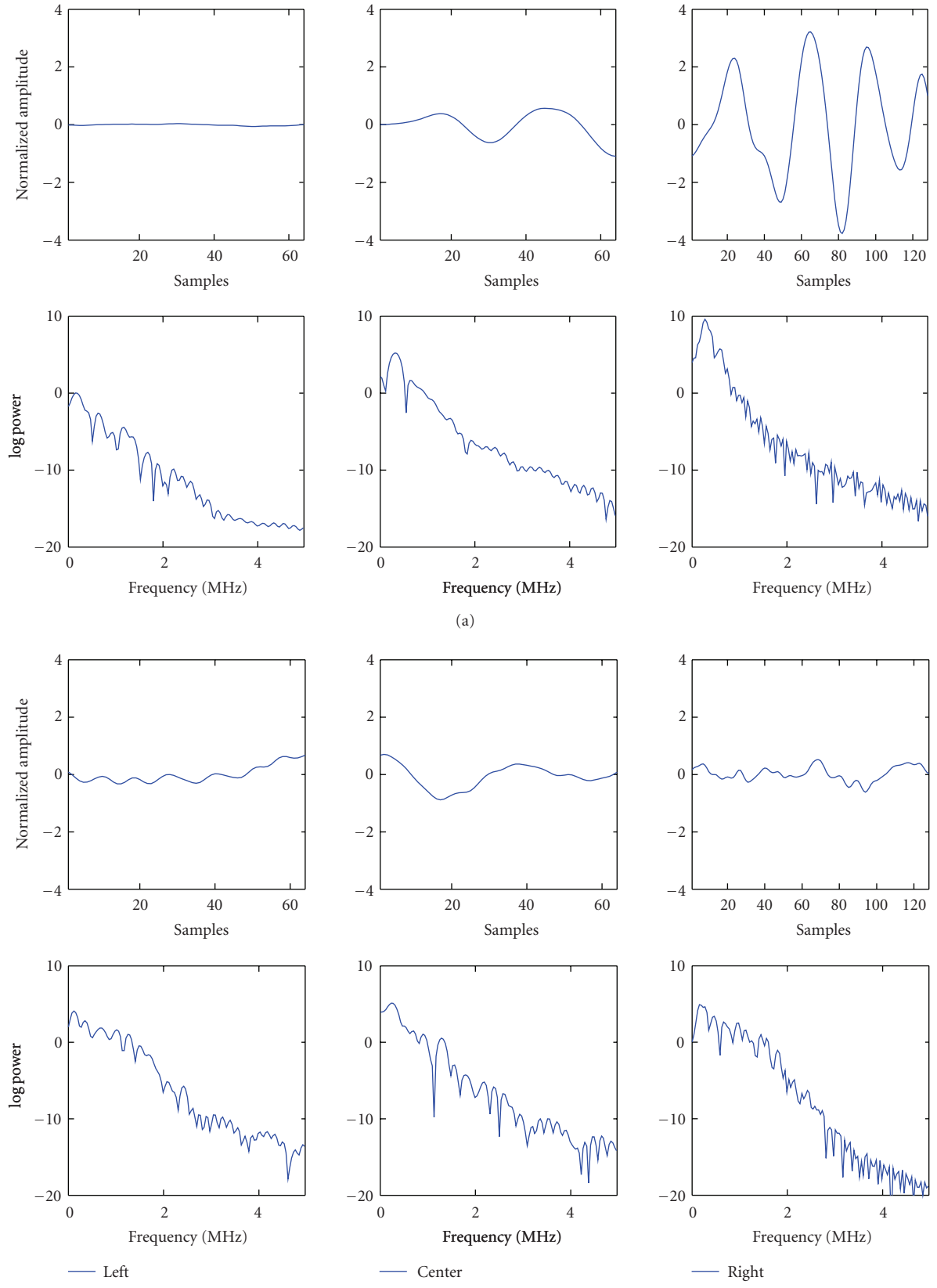

Figure 6: (a) Waveforms and log power spectra of 64-sample long time window preceding the P-wave, centered around P-wave, and a 128-sample long window after the P-wave; (b) Raw data and spectra of noise segments that may be recognized as a pseudo-P-wave.

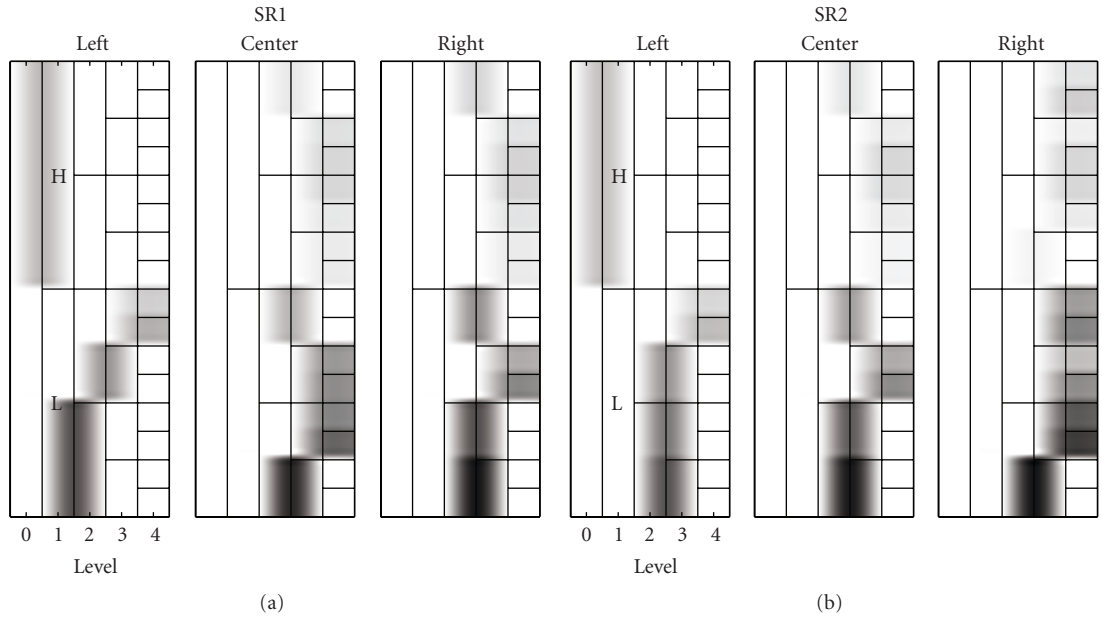

Figure 7: The WP subband tiling for datasets SR1 (a) and SR2 (b). Each selected subband is weighted with the corresponding log scaled Euclidean distance between classes. The darker nodes have higher discrimination power.

band was selected as one feature in the left window. The discriminative power of the high band in the left window was higher than the high subbands in the center and right windows, whereas the discriminatory power of the center and right windows in lower bands were much higher than the left window. Interestingly, finer levels were selected in the center and right windows.

4.3. AR Model-Based Features. The AE data were also analyzed in the left, center, and right windows using an autoregressive model. Since the P-waves and oscillations following them are more structured, it is expected that the AE waveforms can be well predicted by a linear combination of the past samples. However, for noise, such a prediction is expected to fail due to the lack of correlation and/or structure between consecutive samples. With this motivation, the prediction error of the AR (alternatively the linear predication) model was used in each time window as another feature for detecting the P-waves. Prior to employing the AR modeling in each window, the data were normalized to zero mean and unit variance in order to eliminate the energy differences between different events. Since short data segments are analyzed, the order of the AR model was investigated with a corrected Akaike information criterion (AICc) of [13],

$$\begin{aligned} \mathrm{AIC} &= -2\log(e) + 2p, \\ \mathrm{AICc} &= \mathrm{AIC} + \frac{2p(p+1)}{N-p-1}, \end{aligned} \tag{2}$$

where p is the model order, N is the sample size, and e is the prediction error of the model. The AICc has a second-order correction for small sample sizes. As the number of samples gets large, the AICc converges to AIC; therefore, it can be employed regardless of sample size [13]. In Figure 8, we present the averaged AICc of both datasets SR1 and SR2 computed in all windows. The AICc criterion indicated a model order between 6 and 8. To obtain an idea about the discriminative power of the selected model order, the receiver operating characteristic (ROC) curves computed on the training data were also constructed in these three consecutive time windows for each model order. The area between the ROC curve (AUC) and the diagonal, no decision, line was used as a measure to quantify the discrimination performance of the extracted features. We also inspected change in discriminatory information as a function of model order in each analysis window (see Figure 8(b)). However, the AUC plot suggested lower model orders, where the model order of $p = 6$ provided maximum discriminatory information.

The ROC curves of different time windows for both datasets are given in Figure 9. It was observed that the area under the curve was the maximum in the time window following the P-wave. This was followed by the window covering the P-wave. Specifically, the prediction error of the model was smaller in the last two windows for real P-waves and provided better discrimination. This is an expected outcome since the signals in these windows have higher SNR and are more structured compared to the signals in the first window.

For each time point, computing the features described could be a demanding process. To reduce the number of candidate time points that need to be tested for P-wave arrival, first the signal was normalized, and then the envelope of the signal was computed with the Hilbert transform. When the envelope of the signal exceeded a predefined threshold, and then that time point was tested for P-wave

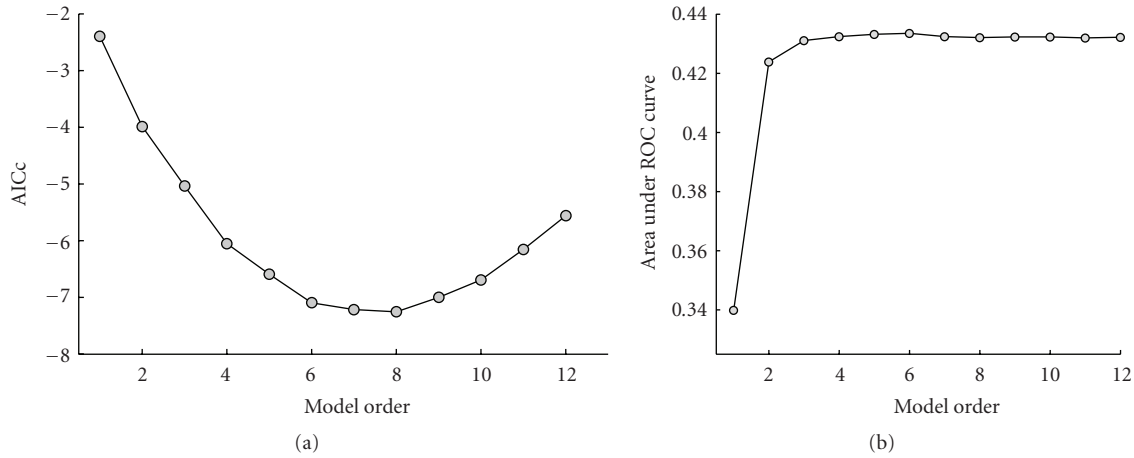

Figure 8: (a) The corrected Akaike Information criterion is computed for both datasets SR1 and SR2 and then averaged. The AICc criterion indicated a model order between 6 and 8, where the minimum was at $p = 8$. (b) ROC curve related to prediction error of the AR model on the training data was computed in the center and right windows and averaged over both datasets SR1 and SR2.

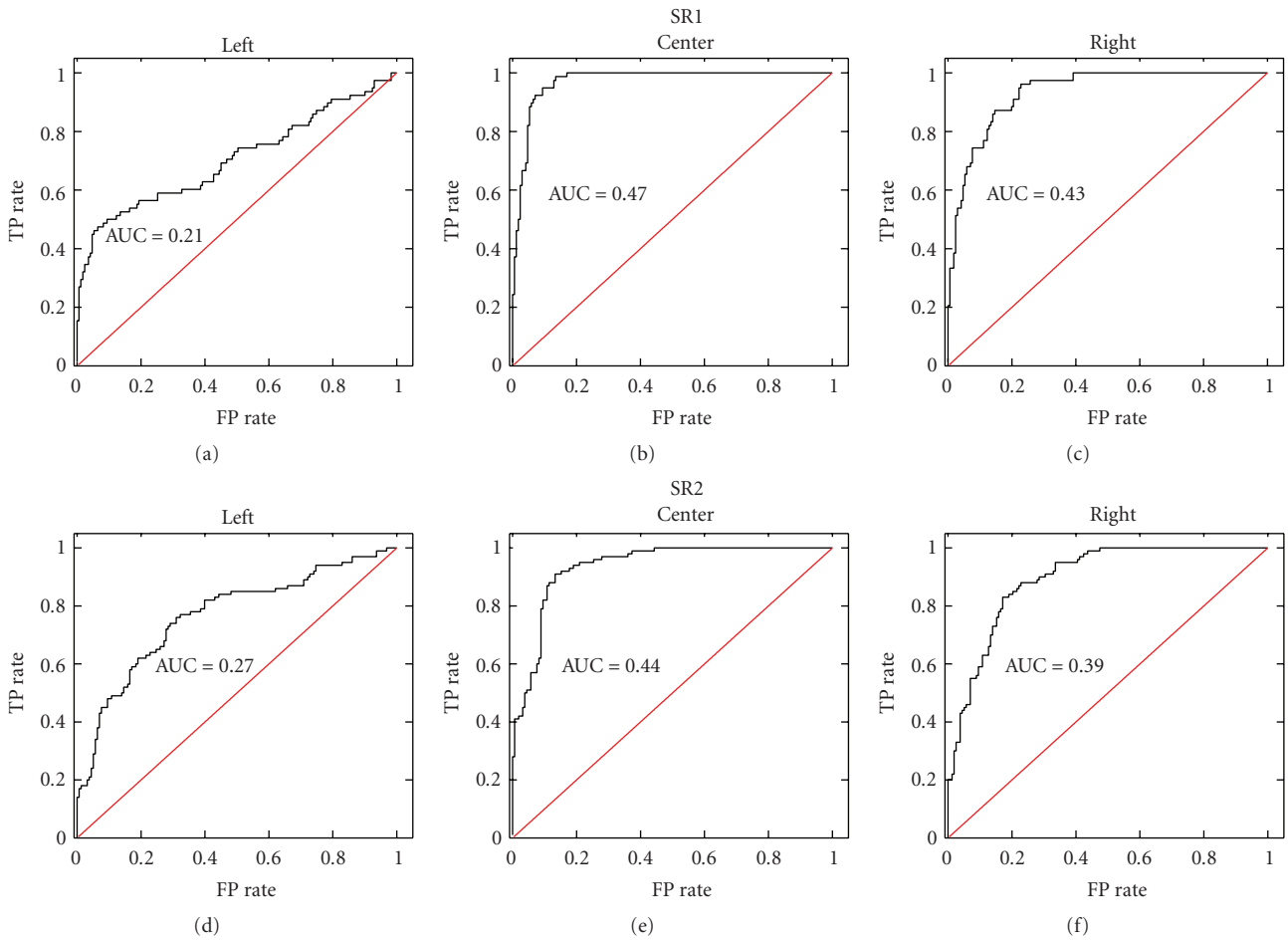

Figure 9: The ROC curves related to the model order $p = 6$ computed on the training data in the left, center, and right windows. Note that the discrimination in the center and right windows is better than the left window.

arrival, it was found that a threshold value of 0.5 was good enough to determine most of the P-waves. The feature vectors for each method presented above were individually fed into a linear support vector machine classifier for the final decision [6]. The main motivation for using an SVM classifier is based on its robustness against outliers and its generalization capacity in higher dimensions, which is the result of its large margin. Furthermore, the output of the SVM classifier was postprocessed by a sigmoid function to map the SVM output into probabilities. This was accomplished by minimizing the cross-entropy error function as suggested in [14]. By using this procedure, we were able to assign posterior probabilities to SVM output which is later used as a confidence level to detect P-wave arrival. The SVM classifier was trained by selecting around 20 multichannel "super" AE events from each data set. Since each event includes AE data from 8 channels, this resulted in 160 P-waves to be tested in each dataset. This number included those clusters with low number of members. However, due to poor SNR, we were unable to visually identify the location of all P-waves in these data sets. Consequently, we selected those events which have a visible P-wave. The training feature vectors for P-waves and noise sets were constructed from this subset by manually marking the P-wave arrivals and noise events that exceeded the predefined threshold in each channel. The numbers of visually identified P-waves were 100 and 78 in datasets SR1 and SR2, respectively. The numbers of noise events were 155 and 162 for SR1 and SR2, respectively. The SVM classifier was trained on the features using the data set of one of the experiments and applied it on the other dataset. In this way, it was guaranteed that no test samples were used in training the classifier. In addition, using such a training strategy, it was investigated whether both data sets share similar patterns. The success of such a strategy can also validate the generalization capability of the classification system constructed.

5. Results

As a first step, on each training set, the decision characteristics of the SVM classifiers were examined by visualizing the ROC curves related to their outputs. We individually investigated the ROC curves of each feature extraction method described above and computed the area between the diagonal line. In addition, we also considered the classification performance of SVM when the raw AE data in these consecutive windows are applied. The ROC curves related to the training data for SR1 and SR2 are depicted in Figure 10. We note that the maximum area in both datasets were obtained with the WP method (0.496 for dataset SR1 and 0.481 for SR2). The second most discriminative features were Mel scale subband energies obtained with FFT (AUC = 0.489 and 0.477 for datasets, SR1 and SR2, resp.). On both datasets, adaptive selection of frequency subbands provided better performance. We note that the SVMs trained with 256-dimensional raw AE data had quite poor performance, where the AUC was 0.39 and 0.31 for datasets SR1 and SR2.

We also examined the performance of a combination of feature sets. Interestingly, the features computed with WP method did not provide any better discrimination performance when they are combined with other features. For dataset SR1, the best performance was obtained with those features computed with WP method only. We note that the best separation performance was obtained with the combination of Mel Scale, AR model error, and spectrum variance features on the dataset SR2 (AUC = 0.483). Based on these observations, we trained the SVM classifiers either with only WP features or with the combination of Mel Scale, AR model error, and spectrum variance features. These classifiers were applied on the test samples we describe below.

In this study, it is desirable to have a system with low false positive rates since there exist several peaks in the baseline preceding the P-waves that can be potentially recognized as a P-wave. For this particular purpose, we used the probability output of the SVM classifier. We only accepted those points as P-Wave arrivals when the posterior probability exceeds a threshold of 0.9. The threshold can also be moved to more stringent levels. However, this may result in the classifier missing the P-waves which will yield low TP rates. One can also select that time as P-wave arrival point, where the posterior probability of the SVM classifier is maximum on the whole AE signal. However, this caused the system to miss the P-waves and identify those regions in the post-P-wave as they share similar characteristics. Therefore, we selected the first point as P-wave when the posterior probability exceeded the 0.9 threshold.

As indicated in earlier sections, the SVM classifier was trained on the features using the data set of one of the experiments and applied on the other dataset. Using this strategy, we evaluated the generalization capacity of the system on similar specimens. At this point, it is difficult to numerically quantify the classification accuracies of both datasets due to the lack of true labels of the test data. The true labels can be obtained by manually marking the P-waves. However, several clusters with low number of members had poor SNR. It was difficult to visually identify the P-waves in these records. Consequently, we elected to study the classification accuracy on those clusters with four or more members. The algorithm identified 13 and 9 clusters with four or more members in the datasets SR1 and SR2, respectively. The super AEs obtained from these clusters had much higher SNR, and the P-waves were mostly visually observable. We manually marked the locations of P-waves and when the classifier identified a region in ± 10 samples around the marked location. We provided such a tolerance region because the P-wave location was not clearly visible on small number of records due to low SNR, and the expert manually marked these positions as possible P-wave location. The success of the system in recognizing the P-waves with WP features was 97.1% when SR2 was used as training and SR1 as testing set. While using SR1 as training and SR2 as testing set, the success on recognizing the P-waves was 94.5%. The combination of features yielded classification accuracies of 93.3% and 94.5% using the same training and testing procedure for these datasets, respectively. We note that similar recognition accuracies were obtained with

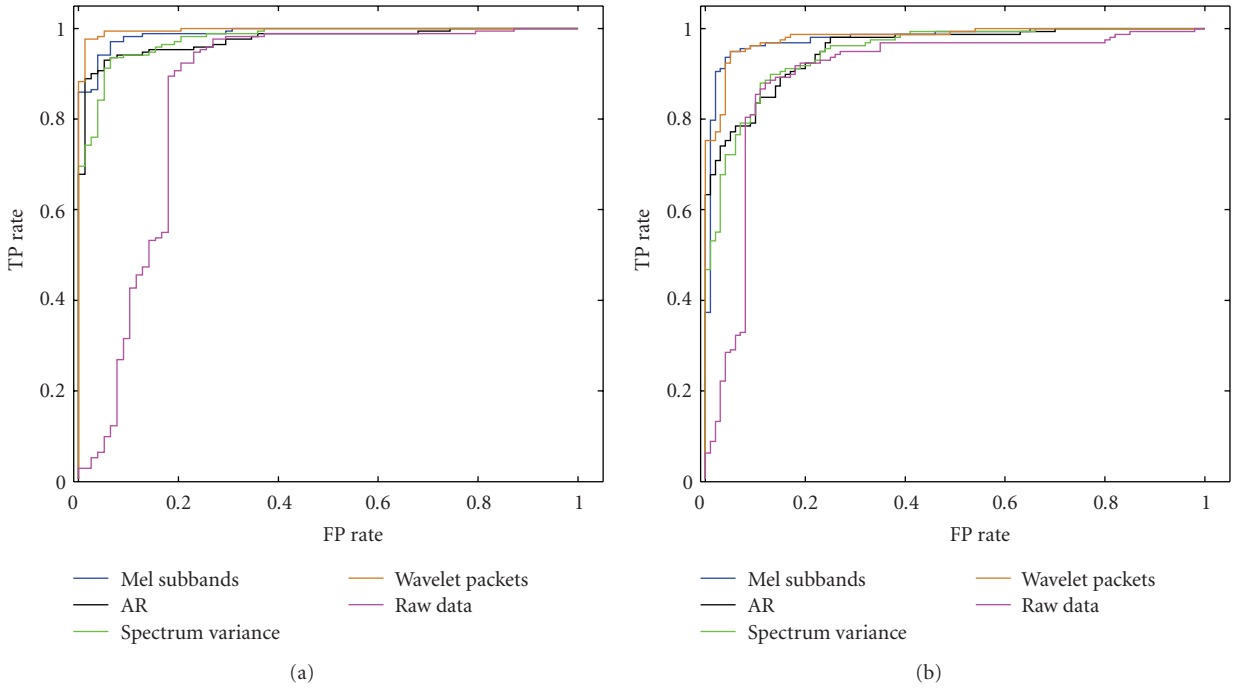

Figure 10: The training classification performance of different feature sets on the dataset SR1 (a) and SR2 (b). The best performance was obtained with WP approach. The performance of the raw AE data was quite poor compared to other methods.

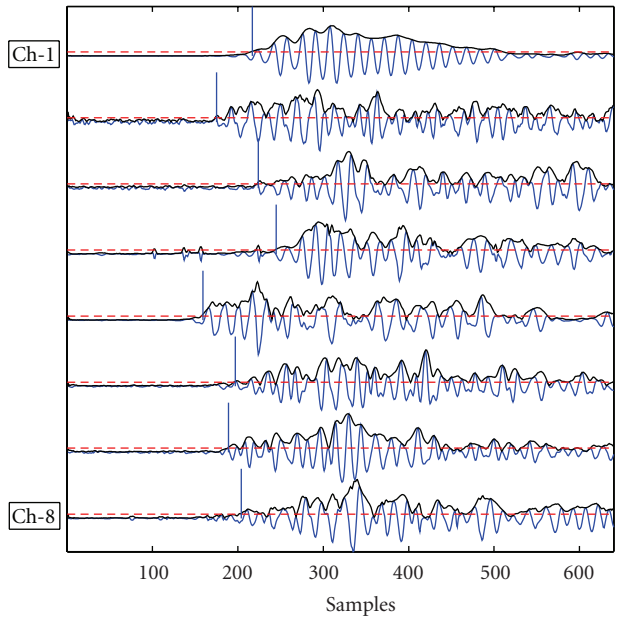

Figure 11: Sample cluster average and detected arrivals from eight sensors of SR1. TOA is marked with a vertical line on each channel. Note that the SVM classifier was trained on SR2.

both techniques, and the performances were in accordance with the training data characteristics. Sample TOA estimates detected by the tuned SVM classifier for a particular cluster are visualized in Figure 11. The horizontal dashed lines represent the predefined threshold. Those time points, where the envelope of the signal exceeded the threshold, were tested for P-wave arrival. The vertical blue lines represent the detected P-wave arrivals. Note that, although several other time points exceeded the threshold, the algorithm successfully eliminated them. Recall that the SVM classifiers were trained with different data sets. It was observed that the SVM classifier successfully recognized the P-waves showing that the classifier can generalize similar specimens. This may provide great advantage in the deployment of the system in real-life applications.

After calculating the arrival information for each sensor, the iterative algorithm in [15] was used to estimate the 3D hypocenter of the source. For the iterative localization method, the location errors were described by the symmetric covariance matrix. The algorithm was executed in a two-step procedure to improve estimation accuracy. In the first step, the iterative method computed an optimized AE position while the covariance matrix that contains spatial variance of arrival times was examined. The two channels that provided largest estimated location errors computed from residual times were disregarded. Then, in the second step, the source location was estimated with the remaining channels. If no noticeable reduction was observed, the location estimation was implemented using all available channels. With this strategy, we evaluated arrival information from the combination of AE sensors. It should be noted that the AE location error for the iterative algorithm tested with synthetic data is generally between 0.5 and 3.0 mm if the P-wave arrivals can be located within ± 10 samples. Figure 12 shows the estimated locations of all clusters and those with at least four members. In Figure 13, we present the photos of

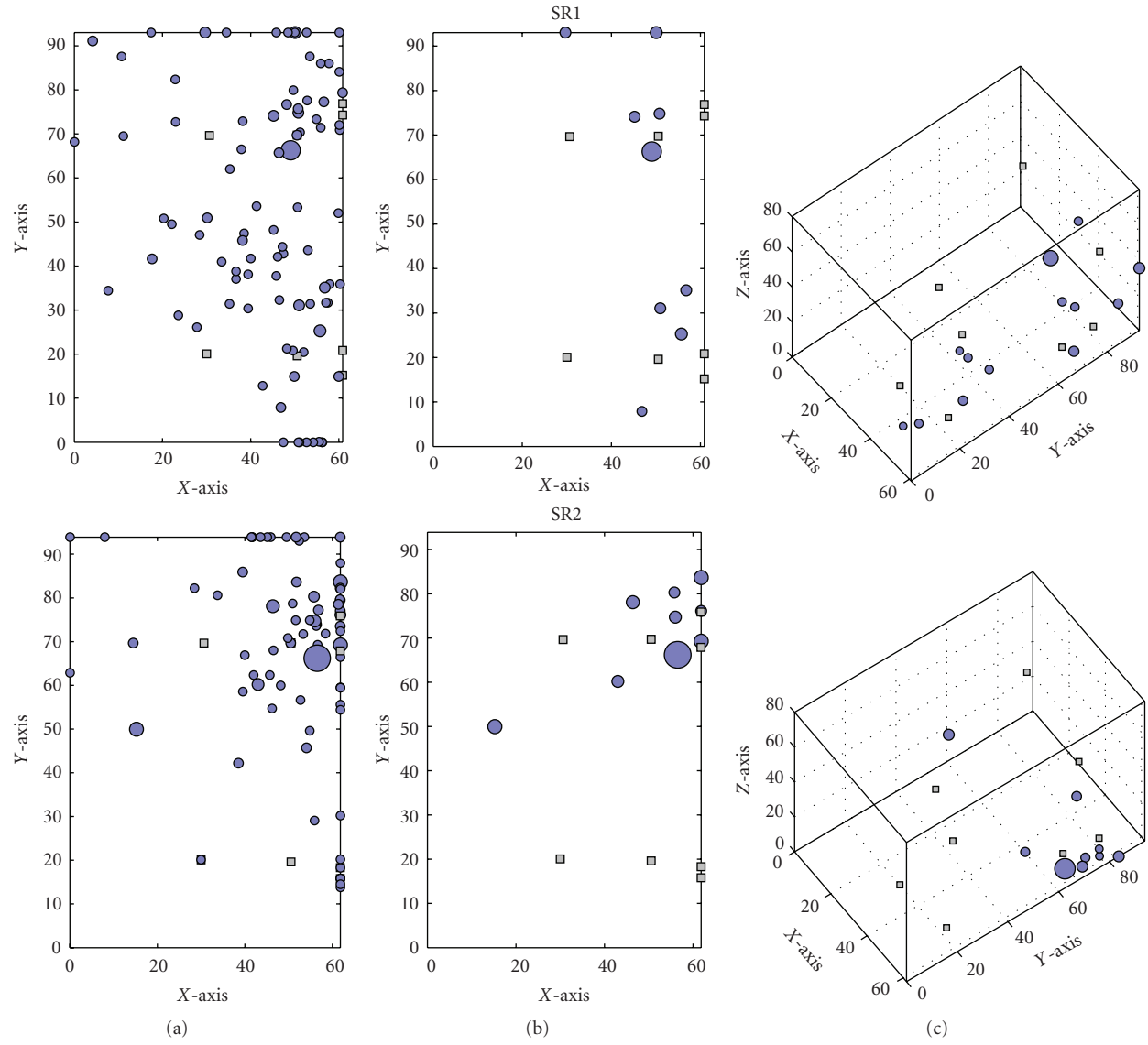

Figure 12: Estimated locations of the AE events for SR1 (first row) and SR2 (bottom row). Each blue circle represents the location of a particular cluster. The diameter of the circle is proportional to the number of AE in the cluster: (a) The locations of all clusters; (b) the locations of those clusters with at least four members. Note that the locations are very close to the free surface; (c) the 3D view of the locations given in the second column.

deformed specimens. The locations were estimated using the WP features for SR1 and combined feature set for SR2. Note that the clusters with at least four members have an SNR that is two times larger than individual recordings. The positions of the AE sensors were marked with the gray squares. Each blue circle represents the location of a particular cluster. The size of each circle is proportional to the number of AE events within the cluster. The locations of the AE events were in accordance with the visible crack locations. Most of the events were localized towards the free surface on both specimens. Interestingly, the largest clusters were localized a few millimeters away from the free surface, which matched well with the observed cracks on the deformed specimens in both tests (Figures 12(b), 13(a), and 13(b)). Several cracks were developed on or adjacent to the frontal surface in the X-Y plane in both tests (Figures 13(a) and 13(b)). Especially for SR2, most clusters were located in the region of $X > 45$, $Y > 60$, $Z < 40$ mm, which precisely matched with the heavily cracked zone observed on the Y-Z plane (lower row in Figures 12(c) and 13(c)).

The locations of all detected clusters in SR1 spread over the specimen with a tendency towards the free surface (Figure 12(a)). This is an expected factor since those clusters with low number of members have lower SNR. It is also possible to capture noise by chance with a low number of members. In order to get around this problem, one can construct another decision system in order to discriminate between AE and noise. Observations indicate that keeping

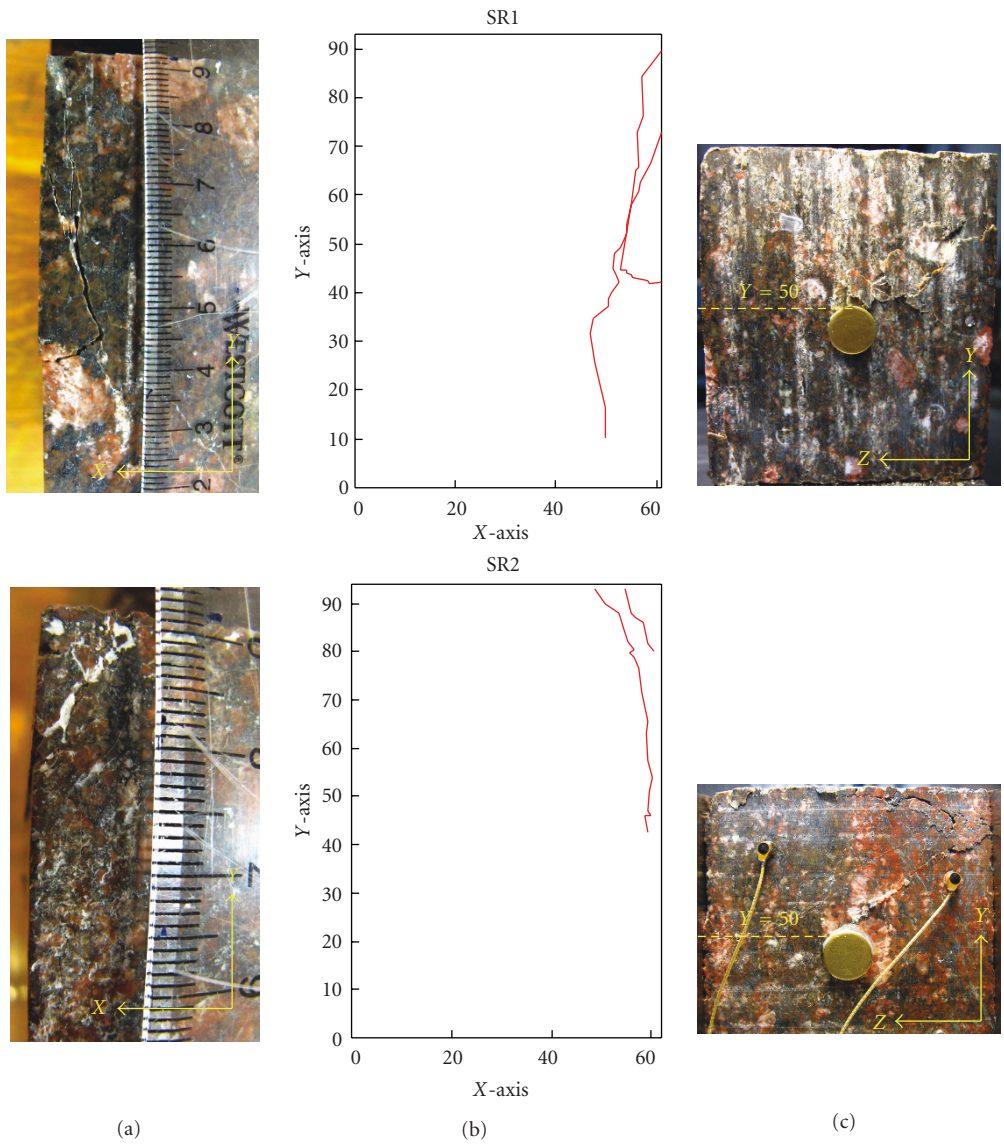

FIGURE 13: (a) Photos of the observed cracks at the upper part of the free surface ($X = 62$ mm). (b) The observed cracks mapped onto X-Y plane, where the free surface is on the right-hand side ($X = 62$ mm). Note that the cracks on SR2 sample are hairline thin. (c) Photos of the observed cracks on the $Z = 80$ mm surface.

those clusters with large number of members automatically eliminates those recordings with noise or random nature. One can also increase the correlation threshold for identifying the clusters. However, there is a chance that a high correlation threshold may erase all possible clusters in the data, where the SNR is low. On the other hand, keeping it very low relaxes the constraints, where the chance of obtaining clusters with noise members is increased. The threshold can be adjusted depending on the quality of the available data.

In order to obtain an idea about the improvement in estimating the location of AE with our technique, we compared our results to the AE locations estimated using the classic threshold algorithm. The traditional algorithm uses an amplitude threshold method to examine P-wave arrivals. The threshold is determined from the mean signal noise (i.e., pre-trigger signal) plus/minus 4 times of the standard deviation or a minimum of ± 2 mV. In order to qualify the picked time mark as a P-wave arrival, two criteria have to be satisfied.

(i) Once the signal exceeds the threshold, it has to surpass the threshold at least 3 times in the subsequent 40-sample (40×50 ns $= 2\,\mu$s) window.

(ii) After 120 samples (i.e., $6\,\mu$s) from the picked time mark, the signal has to exceed threshold at least once.

The threshold method has been studied and proven reliable [16] and was chosen due to its simplicity and efficiency to process thousands of AE events. In Figure 14, we provide the estimated locations with the traditional threshold method. We note that the threshold method resulted in a very scattered pattern of those AE events and did not provide

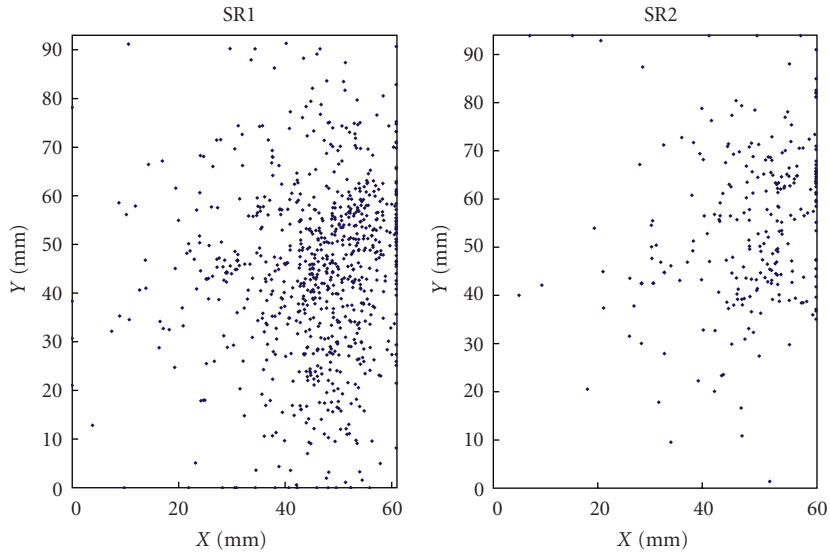

Figure 14: AE locations calculated with classic algorithm on SR1 and SR2 without clustering analysis and SVM technique.

clear information on crack locations. This was due to the raw AE signals being quite noisy and the TOA that was not precisely detected by the simple threshold-passing criterion. The proposed machine learning approach, however, proved its strength and potential to filter out the noise and enhance the SNR to correctly identify the position of major cracks.

6. Conclusions

Novel approaches based on hierarchical clustering and support vector machines (SVM) are introduced for clustering AE signals and detecting P-waves for microcrack location in the presence of noise. Prior to feature extraction and classification process, spikes from the AE data are removed by employing a median filter. Clusters of AE events are identified by inspecting their pairwise correlation. After identifying clusters, an averaging step was implemented to obtain "super" AE with improved SNR. Characteristic features were extracted from the data in time and frequency domains to identify P-waves for time of arrival (TOA). SVM classifiers with probabilistic outputs were trained with these features to recognize P-waves for TOA determination. The location of each AE cluster was estimated accordingly.

The proposed machine learning technique with clustering analysis and SVM showed that the estimated clusters can successfully indicate the location of failure observed in surface instability tests, in which the cracks were promoted to occur close to the front free surface of the specimen. This approach, compared to the classic AE algorithm that gave a very disperse pattern and was not indicative of the region of failure, also presents the capability of filtering noisy signals and enhance the SNR to obtain more reliable AE cluster locations. The preliminary results show that the method has the potential to be a component of a structural health monitoring system.

Acknowledgments

Partial support was provided by the National Science Foundation, Grant no.CMMI-0825454. The authors express their appreciation for the constructive comments provided by the referees, which served to considerably improve the paper.

References

[1] C. Grosse, S. D. Glaser, and M. Krüger, "Wireless acoustic emission sensor networks for structural health monitoring in civil engineering," in *Proceedings of the European Conference on Non-Destructive Testing (ECNDT '06)*, pp. 1–8, Berlin, Germany, 2006.

[2] L. Golaski, P. Gebski, and K. Ono, "Diagnostics of reinforced concrete bridges by acoustic emission," *Journal of Acoustic Emission*, vol. 20, pp. 83–98, 2002.

[3] V. Emamian, M. Kaveh, A. H. Tewfik, Z. Shi, L. J. Jacobs, and J. Jarzynski, "Robust clustering of acoustic emission signals using neural networks and signal subspace projections," *EURASIPJournal on Applied Signal Processing*, vol. 2003, no. 3, pp. 276–286, 2003.

[4] Z. Gong, E. O. Nyborg, and G. Oommen, "Acoustic emission monitoring of steel railroad bridges," *Materials Evaluation*, vol. 50, no. 7, pp. 883–887, 1992.

[5] C. U. Grosse, F. Finck, J. H. Kurz, and H. W. Reinhardt, "Improvements of AE technique using wavelet algorithms, coherence functions and automatic data analysis," *Journal of Construction and Building Materials*, vol. 18, no. 3, pp. 203–213, 2004.

[6] T. Hastie, R. Tibshirani, and J. Friedman, *The Elements of Statistical Learning*, Springer, New York, NY, USA, 2001.

[7] N. Iverson, C.-S. Kao, and J. F. Labuz, "Clustering analysis of AE in rock," *Journal of Acoustic Emission*, vol. 25, pp. 364–372, 2007.

[8] S. Theodoridis and K. Koutroumbas, *Pattern Recognition Second Edition*, Academic Press, New York, NY, USA, 2003.

[9] M. Y. Park, T. Hastie, and R. Tibshirani, "Averaged gene expressions for regression," *Biostatistics*, vol. 8, no. 2, pp. 212–227, 2007.

[10] A. E. Cetin, T. C. Pearson, and A. H. Tewfik, "Classification of closed and open shell pistachio nuts using principal component analysis of impact acoustics," in *Proceedings of the IEEE International Conference on Acoustics, Speech, and Signal Processing (ICASSP '04)*, pp. 677–680, May 2004.

[11] N. Saito, *Local feature extraction and its applications using a library of bases*, Ph.D. thesis, Department of Mathematics, Yale University, New Haven, Connm USA, December 1994.

[12] N. F. Ince, F. Goksu, A. H Tewfik, I. Onaran, A. E. Cetin, and T. Pearson, "Discrimination between closed and open-shell (Turkish) pistachio nuts using undecimated wavelet packet transform," *Biological Engineering Journal, American Society of Agricultural and Biological Engineers (ASABE)*, vol. 1, no. 2, pp. 159–172, 2008.

[13] K. P. Burnham and D. R. Anderson, *Model Selection and Multimodel Inference: A Practical Information-Theoretic Approach*, Springer, New York, NY, USA, 2nd edition, 2002.

[14] J. C. Platt, "Probabilistic outputs for support vector machines and comparisons to regularized likelihood," in *Advances in Large Margin Classifiers*, A. Smola, P. Bartlett, B. Schölkopf, and D. Schuurmans, Eds., MIT Press, Cambridge, Mass, USA, 1999.

[15] J.H. Kruz, S. Koppel, L. Linzer, B. Schechinger, and C. U. Grosse, "Source localization," in *Acoustic Emission Testing: Basics for Research-Applications in Civil Engineering*, C. U. Grosse and M. Ohtsu, Eds., chapter 6, Springer, Berlin, Germany, 2008.

[16] K. R. Shah and J. F. Labuz, "Damage mechanisms in stressed rock from acoustic emission," *Journal of Geophysical Research*, vol. 100, no. 8, pp. 15527–15539, 1995.